Subdiffraction-Limited Far-Field Raman Spectroscopy of Single Carbon Nanotubes: An Unenhanced Approach

Ifat Kaplan-Ashiri, Eric J. Titus, and Katherine A. Willets*

Department of Chemistry and Biochemistry, The University of Texas at Austin, 1 University Station A5300, Austin, Texas 78712, United States

ABSTRACT We present a new approach for subdiffraction-limited far-field Raman spectroscopy of single carbon nanotubes using through-the-objective total internal reflection (TIR) excitation coupled to an atomic force microscope (AFM). By using this approach, we are able to detect spectroscopic signatures of structural changes along a single nanotube with nanometer resolution. A single multiwalled carbon nanotube is mounted on an AFM tip and imaged while tapping on the surface of a glass coverslip. As the angle of incidence of the excitation field is changed, we are able to tune the penetration depth of the evanescent field by steps as small as 2−10 nm. An increase in the ratio of the Raman D band (the disorder band) to G band (the in-plane graphitic band) of the carbon nanotube was demonstrated as the penetration depth decreased, indicating that most defects are concentrated at the end of the nanotube. We also observed frequency shifts of the G band as we changed the penetration depth. By changing the polarization of the incident beam, we are able detect the orientation and possible local curvature in the nanotubes. Coupling through-the-objective TIR with AFM is a powerful technique for studying structural and chemical properties of carbon nanotubes and can be easily extended to many other nanoscale/molecular systems.

KEYWORDS: carbon nanotube · Raman · subdiffraction-limited · AFM

The correlation between the chemical and structural properties of molecular and nanoscale systems, together with the ability to control and change their environment, is of great importance for many studies in chemistry and biology. Nanometer and molecular scale studies require high-resolution imaging capabilities that can readily be achieved by electron and scanning probe microscopes[1,2] but are more challenging to achieve using optical techniques. While electron microscopes provide detailed structural and morphological information at the nanometer length scale, they operate at high voltage and under vacuum, limiting the types of samples that can be analyzed by this technique. Scanning probe microscopes can be operated in a wide variety of environments and provide us with detailed morphological information, but their ability to provide chemical information is limited.[3] Optical microscopy and spectroscopy, on the other hand, have the ability to provide information on molecular structure and composition; however, optical imaging suffers from diffraction-limited resolution and cannot resolve details smaller than 0.61λ/NA or roughly half the wavelength of the illumination source. Despite this fundamental resolution limit, optical imaging and spectroscopy methods are of great importance in chemistry and biology because they are relatively fast and nondestructive characterization techniques.

Recently, several far-field optical microscopy techniques have been developed in order to defeat the diffraction limit, including stimulated emission depletion (STED) microscopy,[4] stochastic optical reconstruction microscopy (STORM),[5] and photoactivated localization microscopy (PALM).[6] All three techniques are fluorescence-based, taking advantage of the inherent photophysics of the fluorophores in the system (either through stimulated emission or blinking/photoswitching of the dyes), to obtain super-resolution optical images. Sub-20 nm resolution is routinely achieved using these far-field techniques, which are competitive with near-field optical microscopy approaches such as near-field scanning optical microscopy (NSOM), tip-enhanced near-field optical microscopy (TENOM), and tip-enhanced Raman scattering (TERS).[3−14] Unlike the near-field approaches, the far-field techniques do not require a sharpened probe to be in close proximity to the sample, which is a significant advantage when sample perturbation is of concern. However, the near-field techniques can be broadly generalized to different forms of optical microscopy, including fluorescence,[15−18] IR,[19−21] and Raman,[3,12,22,23] while examples of nonfluorescence-based, super-resolution far-field imaging are rare.[24]

In this paper, we describe a new approach for studying subdiffraction-limited structural disorder in single multiwalled carbon

*Address correspondence to kwillets@mail.utexas.edu.

Received for review September 22, 2010 and accepted January 5, 2011.

Published online January 13, 2011
10.1021/nn102498h

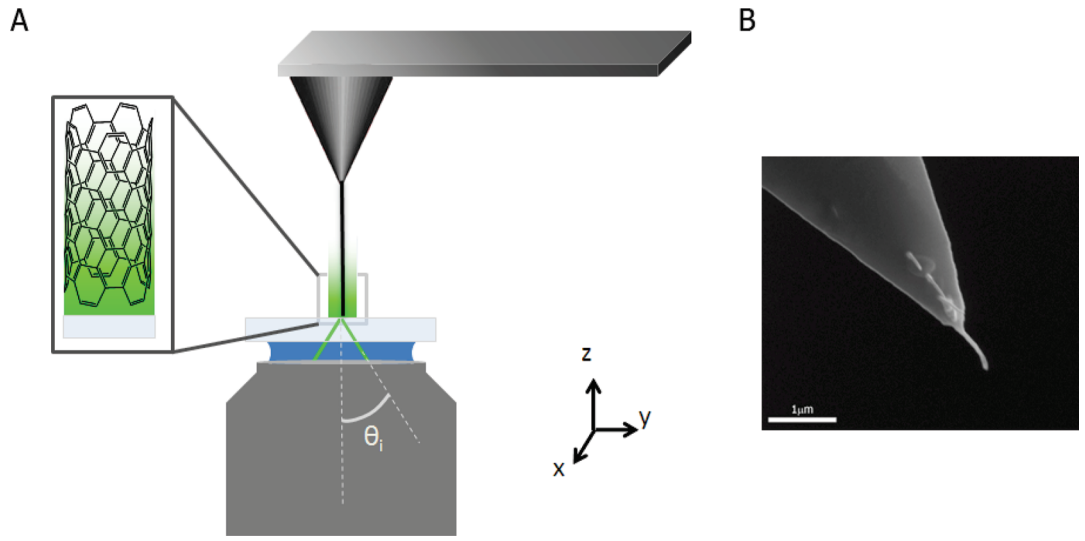

Figure 1. (A) General schematic of the experiment. An AFM is coupled with an optical microscope based on through-the-objective TIR for Raman excitation. The AFM tip is functionalized with a single carbon nanotube, which is excited by the TIR evanescent field, and its Raman scattering is detected. The penetration depth of the evanescent field is tuned by adjusting the angle of incidence (θ_i) of the excitation beam. (B) AFM tip functionalized with a single carbon nanotube.

nanotubes using a far-field Raman imaging technique based on through-the-objective total internal reflection (TIR). Carbon nanotubes are well-studied in the literature and have a host of interesting mechanical, electronic, and optical signatures that make them potentially useful in a wide array of applications, including field effect transistors,[25] light-emitting diodes,[26] additives to lithium-ion batteries,[27] and multifunctional fillers of composite materials.[28] Carbon nanotubes have also served many times as a case study for near-field techniques including TERS measurements[29,30] as well as simultaneous near-field Raman and photoluminescence studies.[31] Here we use a single carbon nanotube to demonstrate subdiffraction-limited Raman spectroscopy based on coupling through-the-objective TIR excitation with atomic force microscopy (AFM). By exploiting the angle-dependent evanescent field decay length produced by TIR excitation, we are able to tune the Raman excitation field by increments of 2−10 nm and detect changes in the contributions from the Raman scattering of the disorder band of a single nanotube. The approach outlined here is general and can be implemented for the study of many different nanoscale and molecular scale systems.

RESULTS AND DISCUSSION

The super-resolution, unenhanced Raman studies of single multiwalled carbon nanotubes were carried out using a coupled AFM and optical imaging/spectroscopy system, as shown schematically in Figure 1 (a detailed description can be found in the Supporting Information). AFM tips were functionalized with single multiwalled carbon nanotubes *in situ* using a scanning electron microscope (SEM); an example is shown in Figure 1B.[32]

A carbon nanotube functionalized tip was mounted into the AFM and aligned to the optical system using Rayleigh scattering from the AFM tip with white light TIR excitation, before switching to 532 nm laser excitation for Raman spectroscopy.[33] The 532 nm excitation light was introduced *via* a through-the-objective TIR approach,[33−35] producing an evanescent field at the surface/interface that decays axially according to

$$I(z) = I_0 e^{-z/d} \quad (1)$$

where I is the intensity of the excitation light, z is the distance from the interface, and d is the penetration depth of the evanescent wave. By varying the angle of incidence (θ_i) of the excitation light, the penetration depth of the evanescent field can be tuned according to the following equation:[34,35]

$$d = \frac{\lambda_0}{4\pi}(n_1^2 \sin^2 \theta_i - n_2^2)^{-1/2} \quad (2)$$

Here d is the penetration depth, λ_0 is the excitation wavelength, θ_i is the angle of incidence, and n_1 and n_2 are the refractive indices of the two mediums at the interface. In our experiment, TIR occurs at the interface between a glass coverslip ($n_1 = 1.515$) and air ($n_2 = 1$); hence the critical angle above which TIR is produced is $\theta_c = 41.3°$. The angles of incidence of the excitation light were controlled *via* a lens mounted on a micrometer stage and were calibrated using a prism (see Supporting Information).[36] The evanescent field penetration depth was calculated according to eq 1 and ranged from 300 ± 200 to 53 ± 1.6 nm for this set of experiments, allowing us to control the excitation of the nanotube on a length scale well below the diffraction limit of light. The minimum penetration depth studied was determined according to the limitations of our signal-to-noise ratio and the smallest incremental

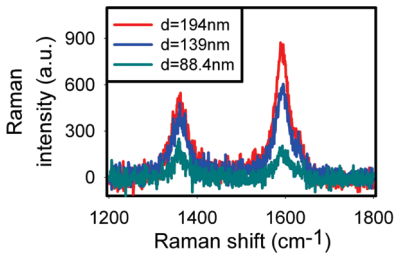

Figure 2. Representative Raman spectra of the multiwalled carbon nanotube shown in Figure 1B at three different penetration depths. The D band appears at ~1360 cm^{-1} and the G band at ~1594 cm^{-1}.

step of the incident angle, *ca.* 0.3°. To eliminate any AFM tip effects on the Raman bands of the suspended carbon nanotube (for instance, any perturbations arising from contact with the AFM tip or any welding materials), the lower limit for the nanotube's length was set to 500 nm, which is almost twice the distance of the maximum penetration depth. (Much longer nanotubes are difficult to work with in AFM, as they tend to be unstable when approaching the surface.[37,38])

Single nanotube Raman spectra from the nanotube shown in Figure 1B were collected at different angles of incidence (and thus, different penetration depths), and several representative spectra are presented in Figure 2. The Raman spectrum of multiwalled carbon nanotubes has two characteristic peaks, the G band at ~1580−1590 cm^{-1} and the D band (the disorder band) at ~1350 cm^{-1}, where G is linked to the graphitic in-plane vibrations (sp^2 hybridization) and D is linked to defects in the structure (in the form of sp^3 hybridization, missing atoms in the lattice, bound species, *etc.*).[39−44] These two peaks can easily be observed in all of the presented spectra for the different penetration depths. This set of data, acquired from a single nanotube tapping on a bare glass surface at a frequency of 260 kHz and an amplitude of 100 nm, demonstrates the ability of our method to detect a suspended nanotube using TIR excitation with no additional signal enhancement. Previous studies have shown that the interactions of single-walled carbon nanotubes with the environment and other neighboring nanotubes directly affect their electronic and optical properties.[45,46] Using our approach, it is possible to isolate the nanotube from its environment and decrease/control contributions from the interactions with the substrate along the length of the nanotube.

The G and D bands in each spectrum were fit as the sum of two Lorentzians with a linear background using a nonlinear least-squares fitting according to

$$I(\tilde{\nu}) = I_{BG,0} + I_{BG,\tilde{\nu}}\tilde{\nu} + \sum_{i=1}^{i=2} I_0 \frac{\left(\frac{1}{2}w_i\right)}{(\tilde{\nu}_i - \tilde{\nu}_0)^2 + \left(\frac{1}{2}w_i\right)^2} \quad (3)$$

where $I_{BG,0} + I_{BG,\tilde{\nu}}\tilde{\nu}$ is a linear frequency-dependent background, I_0 is the height of the peak, w is the width

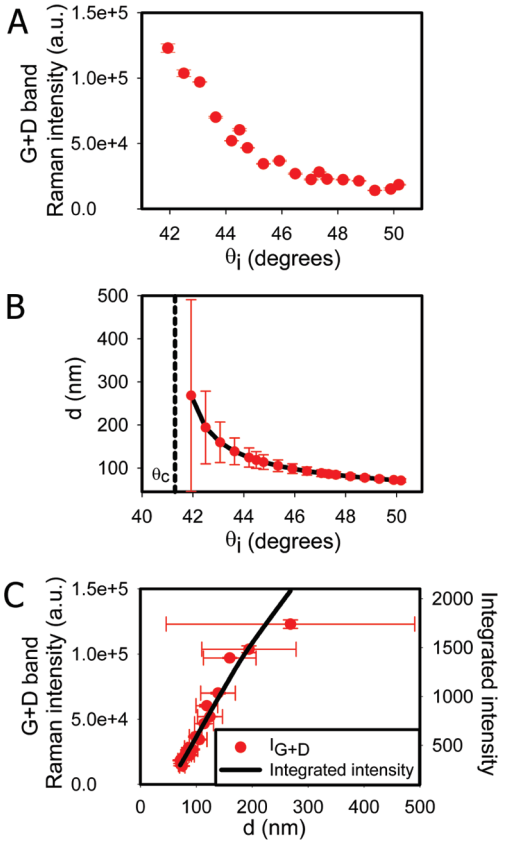

Figure 3. (A) Sum of the G and D band intensities *vs* angle of incidence (θ_i). (B) Calculated penetration depth of the evanescent field *vs* angle of incidence. The critical angle at 41.3° is shown as a dashed line. (C) Sum of the G and D band intensities *vs* the evanescent field penetration depth (red dots) as well as the calculated integrated intensity (see eq 2 in the text) *vs* the penetration depth (black line).

of the peak, and $\tilde{\nu}_0$ is the center frequency of the Lorentzian. From the fit, the integrated intensities of the peaks associated with the D and G bands were calculated (I_D and I_G, respectively) as the area of each individual Lorentzian. The sum of the integrated intensities of the two bands at each angle of incidence is presented in Figure 3A. For comparison, the calculated penetration depth (see eq 2) is also plotted *versus* the angle of incidence (Figure 3B). These results demonstrate that the integrated Raman intensity decays with increasing angle of incidence, following the same trend that is observed for the penetration depth. This correlation verifies that the nanotube was excited axially by the evanescent field.[34,35]

The intensity of the excitation light along the length of nanotube can be estimated by integrating the evanescent field intensity given in eq 1 for different values of the penetration depth. The measured Raman scattering intensities as well as the integrated intensities are plotted *versus* the penetration depth and presented in Figure 3C. It is clear that both the predicted and measured intensities decrease with decreasing penetration depth. Since the collected Raman signal is strongly dependent on the intensity

of the exciting field, this result again confirms that the evanescent field is exciting the Raman scattering of the nanotube along its axis. As the angle of incidence increases and the penetration depth decreases, the fraction of the carbon nanotube that is being probed is decreasing by 2−10 nm increments, well below the diffraction limit of light. Detectable differences in both the Raman intensity as well as the Raman spectra themselves are observed at an acceptable signal-to-noise ratio as we excite increasingly smaller regions of the nanotube.

A closer look at the set of spectra at different penetration depths (see Figure 2) shows that the relative intensities of the G and D bands change as the penetration depth decreases. The ratio of the intensities of the D and G bands (I_D/I_G) *versus* the penetration depth (see Figure 4) shows an increase of the D band (the disorder band) intensity relative to the G band intensity as the penetration depth decreases. Unlike other TIR-based Raman studies, in which only the intensities of the Raman bands changed with different θ_i,[35] here we observe a change in the spectrum itself, which can only be ascribed to differences in the local structure of the carbon nanotube as we change the penetration depth of the field.

To understand how changing the penetration depth can probe local structure of a carbon nanotube, we first need to understand how different segments of the nanotube respond to the excitation field and contribute to the overall Raman intensity. Because the AFM tip is oscillating at 260 kHz with an amplitude of 100 nm, the excitation field appears time varying to the carbon nanotube analyte. We have modeled the effect of this time-dependent excitation on the relative excitation intensity experienced by different fractions of the nanotube (see Supporting Information for full details). In the event that the nanotube is entirely homogeneous, these values would correspond to the relative Raman intensity contributed by each segment. Table 1 summarizes our results for the relative contributions from different segments of the nanotube tip for four different penetration depths. For example, we see that the first 10 nm of the suspended nanotube (*e.g.*, 0−10 nm from the end) would contribute just 4.5% of the overall Raman signal at a penetration depth of 255 nm, while at a penetration depth of 56 nm, that same portion of the nanotube contributes 16.4% of the total signal. As we move further from the end of the nanotube, the contribution becomes much weaker; for example, the portion of the nanotube located 300−310 nm from the end of the tip contributes just 1.4 and 0.08% to the total intensity as the penetration depth is tuned from 255 to 56 nm, respectively. These results show that the signal from the end of the nanotube is 205 times more intense than the segment 300 nm from the end when the penetration depth is small (*e.g.*, 55 nm), compared to only 3 times more intense when the penetration depth is large (255 nm). Thus, as we decrease the penetration depth of our excitation field, we expect the observed Raman signal to be dominated by the end of the tip.

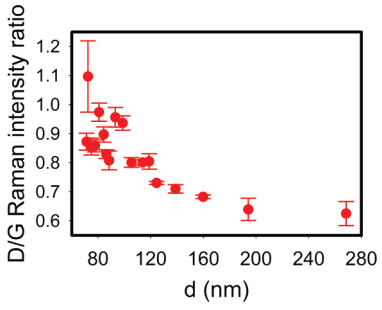

Figure 4. D to G band intensity ratio as calculated from a set of spectra acquired from a single nanotube. The D/G ratio is plotted against the evanescent field penetration depth.

The discussion so far has assumed that the nanotube is unchanging along its length, such that the Raman signal will be proportional to the excitation intensity alone. However, the actual Raman signal we observe is a function of not only the excitation intensity but also the Raman cross section of a particular mode (*e.g.*, D or G) and the density of sites contributing to each mode. Because the Raman cross sections are fixed regardless of penetration depth, the observed change in the I_D/I_G ratio must be due to changes in the density of the defect and graphitic sites along the length of the carbon nanotube. If the defect density is highest at the end of the nanotube, we expect to see a stronger contribution from the D band (and a corresponding reduction in the contribution from the G band) in the case where the end of the nanotube dominates the signal, that is, at the smallest penetration depths. Thus, the fact that the I_D/I_G ratio increases as we decrease the penetration depth (as in Figure 4) indicates that the

TABLE 1. Percent Integrated Incident Intensity on CNT Segments

	CNT segment measured in distance from the end of the nanotube (nm)						
penetration depth (nm)	0−10	50−60	100−110	150−160	200−210	250−260	300−310
255	4.48	3.68	3.03	2.49	2.04	1.68	1.38
98	9.79	5.87	3.52	2.11	1.26	0.76	0.45
65	14.28	6.61	3.06	1.42	0.66	0.30	0.14
56	16.43	6.70	2.73	1.11	0.45	0.18	0.08

structure associated with the end of the nanotube must contain a higher density of defects.

Changes in the D/G Raman intensity ratio due to structural effects have been previously reported in the literature for carbon nanotubes.[44,47,48] For example, Raman studies of superlong (~5 mm) double-walled carbon nanotubes show that the D/G ratio changes significantly as the authors probe different segments of the tube.[49] Many studies on the chemical modification/functionalization of carbon nanotubes have also used Raman to detect changes in the D and G bands due to chemically induced structural changes.[47,48,50] Following nanotube treatment with different acids such as H_2SO_4, HCl, or HNO_3, an increase in the D band relative to the G band is usually observed, as these acids oxidize the nanotube and introduce new defects/sp^3 bonds.[48,51] Other studies have used acid treatments to cut nanotubes and have shown that, as the length of the nanotube decreases, the D/G intensity ratio increases.[47,48,50] These effects are attributed to the ratio of the nanotube edge to its length. The edges of multiwalled carbon nanotubes are known defect sites;[49] thus as the nanotube grows shorter, the edges make a larger overall contribution to the Raman signal and the ratio of the D/G intensity increases.[47,48]

We attribute the observed change in the D/G intensity ratio in our data to the same effect since we are probing a smaller fraction of the nanotube length relative to its edge as the penetration depth decreases. The structural differences associated with these edges behave as defect sites, leading to an increased I_D/I_G as described above. Using traditional far-field microscopy, we would be unable to observe this effect because it becomes prominent only when the penetration depth is below 200 nm, which is below the resolution offered by the diffraction limit of light, for example, $\sim\lambda/2$ (here, roughly, 250 nm). Only when we are able to probe the long axis of the tube at length scales below the diffraction limit do we see the strong contribution of the D band emerge. These results demonstrate the ability of our method to detect local structural changes in the nanotube by using subdiffraction-limited Raman spectroscopy. We are working to develop a quantitative model to determine if we can assign the probability of locating defects at particular locations along the nanotube axis; the results will be the subject of a future publication.

In addition to measuring the changing intensities of the D and G bands, we can also study how the peak frequencies of the bands change as a function of the penetration depth. Shifts in the Raman frequencies of carbon nanotubes have been previously reported and were shown to occur due to changes in excitation energy,[52−54] laser power,[55] temperature change,[55] and nanotube diameter.[56] Tracking the frequencies of both the D and G bands (see Figure 5) shows no dependence on penetration depth for the D band (Figure 5A)

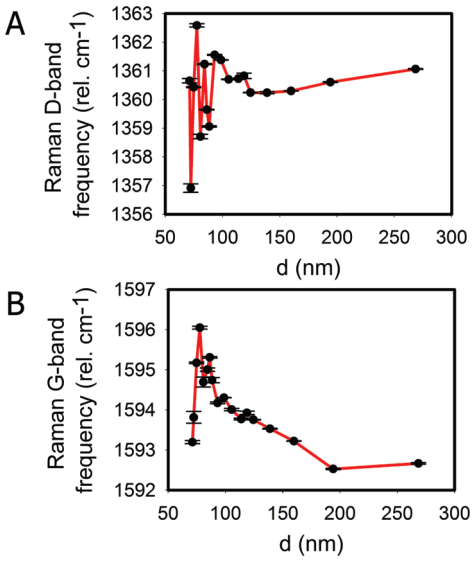

Figure 5. Peak Raman frequency *vs* the evanescent field penetration depth for the (A) D band and (B) G band.

and an upshift for the G band as the penetration depth decreases (Figure 5B). While the lowest penetration depth points (d < 70 nm) of the G band data show a down-shift back to the original peak frequency, it is unclear whether this is a spurious effect due to low signal-to-noise; as such, we cannot assign this to a real effect. Up-shifts in the Raman frequencies of the G band have been demonstrated for double-walled carbon nanotubes with decreasing laser power (a smaller effect was demonstrated for the D band).[46] Here, laser power effects can be translated into the overall decrease of intensity of the evanescent field as the penetration depth decreases (see Figure 3). A similar upshift in the G band was also demonstrated for multiwalled carbon nanotubes with different radii; as the diameter of the multiwalled nanotube decreases, the G band frequency up-shifts while the D band remains relatively unperturbed.[56] Even though we observe no clear change in the nanotube diameter as a function of length based on SEM imaging, diameter effects cannot be completely excluded because of the resolution limit of the SEM (*ca.* 2 nm). However, a decrease in nanotube diameter should also affect the integrated Raman intensity and lead to differences in the behavior between the predicted and measured Raman intensities shown in Figure 3, which we do not observe. Mechanical effects, such as the interaction of the nanotube with a substrate, can also induce spectral shifts.[57] In our case, if there is some sort of interaction between the nanotube end and the glass substrate that leads to a band shift, it would most likely be more pronounced at small penetration depths where the end signal dominates. However, it is unclear why the D band would be unaffected in this case. Although the origin of the band shift effects are only speculated and cannot be positively assigned at this point, these

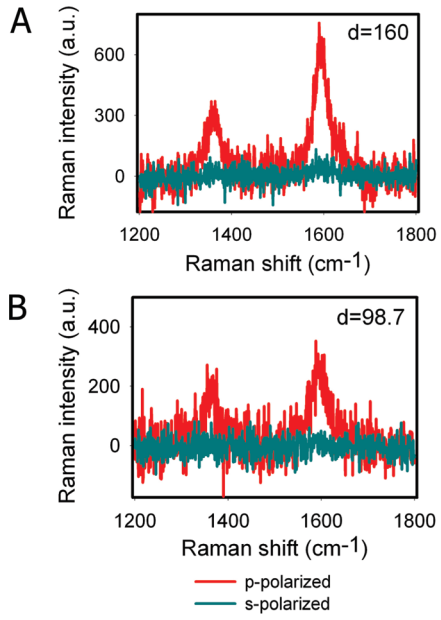

Figure 6. Excitation polarization dependence of the Raman spectra of a single carbon nanotube. The nanotube was excited separately with p-polarized (red line) and s-polarized (blue line) light. Spectra at two different penetration depths are presented, (A) d = 160 nm and (B) d = 98.7 nm.

results still demonstrate that subdiffraction spectroscopy can reveal dynamic changes in the spectral features of single carbon nanotubes that would be hidden using traditional far-field spectroscopy.

All results shown thus far have been obtained for the nanotube shown in Figure 1B excited by p-polarized excitation light. The polarization of the exciting light plays an important role in Raman studies of carbon nanotubes due to their anisotropic structure. The maximum Raman scattering intensity from carbon nanotubes is achieved when the excitation light is polarized along the main axis of the nanotube (in our case, the z-axis).[42,58] To demonstrate this same effect with our system, we compare Raman spectra from our nanotube excited with p-polarized light to spectra excited by s-polarized light (Figure 6). The p-polarized light will have components in both the y- and z-directions (*e.g.*, both orthogonal to and aligned with the nanotube axis, as shown in Figure 1), while s-polarized light will only have a component in the x-direction (orthogonal to the nanotube axis); this allows us to determine whether our geometry is sensitive to the nanotube orientation. Figure 6 shows that, when this carbon nanotube is excited with s-polarized light, we observe no detectable signal, indicating that any polarizable bonds aligned orthogonal to the nanotube axis produce negligible Raman intensity. On the other hand, when the nanotube is excited by p-polarized light, Raman intensity is observed from both the G and the D bands, which is assigned to scattering from polarizable bonds oriented along the nanotube axis, which are preferentially excited by the z-component of the light (with negligible contribution from the y-component). While the polarization dependence of the excitation is expected for the G band, which originates from the graphitic sp^2 carbons of the nanotube, the lack of signal from the D band with s-polarized excitation is less obvious. We postulate that not only are defects concentrated at the end of the nanotube but they are also aligned along the long axis of the nanotube such that they show preferential Raman scattering from z-excitation. We show this for two different penetration depths to illustrate that even when the D band becomes more prominent (at lower values of d) there is no signal observed with s-polarized excitation.

The polarization-dependent results above suggest that we can probe the orientation of a suspended nanotube relative to the surface by changing the polarization of the Raman excitation light. For instance, if the nanotube is perpendicular to the surface (as in Figure 1B and Figure 6), no Raman signal should be detected when the light is s-polarized; on the other hand, if the nanotube is tilted with respect to the surface normal, signal should be detected with s-polarized excitation because the long axis of the nanotube now has an in-plane component in both x and y. Figure 7A emphasizes this idea quite clearly. In this case, the nanotube is not aligned with the surface normal and a substantial signal is detected when the light is s-polarized as well as p-polarized. This tip also shows an increase in the D/G band ratio with decreasing penetration depth for p-polarized excitation, increasing from 0.72 at d = 115 nm to 1.0 at d = 88 nm, as seen previously (*e.g.*, Figure 4). Low signal-to-noise and a diffuse background prevent a similar analysis in the case of s-polarized excitation.

Figure 7B shows a third example in which the nanotube appears to be oriented along the z-axis, similar to the first nanotube tip that was presented (see Figure 1A). However, the polarization study of this nanotube tip shows a completely different behavior, as Raman scattering was observed upon both s- and p-polarized excitation. In this case, the bulk orientation of the nanotube cannot explain the appearance of Raman scattering upon s-polarized excitation, suggesting that the nanotube has some structural feature oriented within the $x-y$ plane that cannot be resolved using SEM. The larger signal from p-polarized excitation is consistent with theoretical predictions, which suggest that the excitation intensity of p-polarized light should be 1.91 and 1.87 times higher than s-polarized light for penetration depths of 90 and 82 nm, respectively.[34] Our results show a similar trend, with ratios between p- and s-polarized intensities of 2.5 and 2.1, respectively. Although these ratios are slightly higher than predicted values, the low signal-to-noise ratios in the s-polarized spectra make it challenging to assign this to a real effect, such as an increased

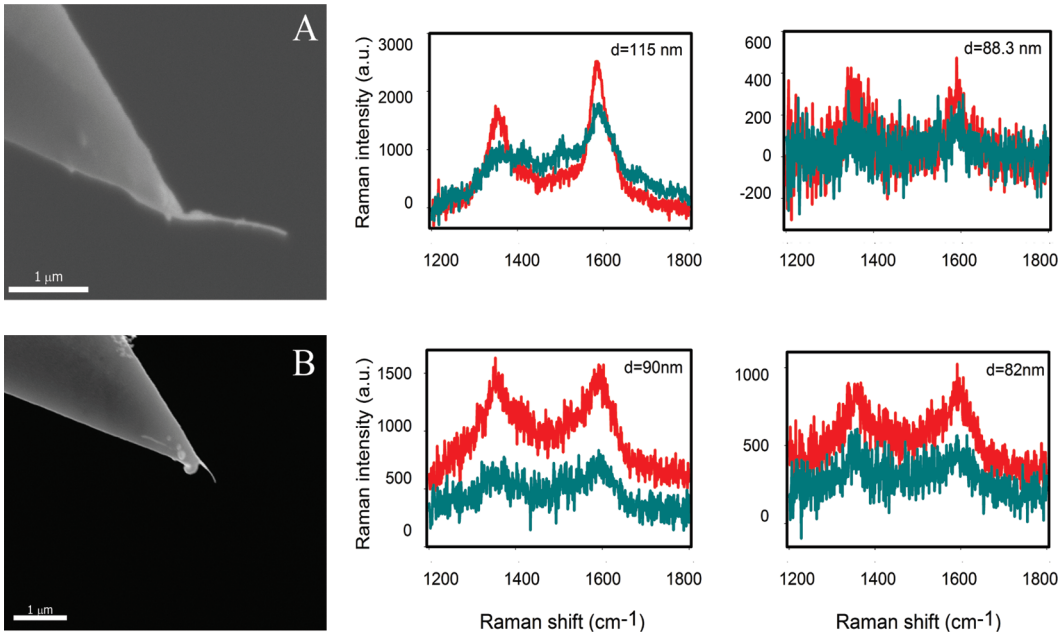

Figure 7. Excitation polarization dependence on nanotube orientation and structure. Sets of spectra for two different carbon nanotubes, each having different orientation and structure, were acquired using both p-polarized (red line) and s-polarized (blue) excitation. For each nanotube, spectra at two different penetration depths are presented.

contribution from the z-polarized component of the p-polarized excitation. We have been unsuccessful obtaining good fits to these spectra, most likely due to the diffuse background which appears in both the s- and p-polarized plots; as such, we are unable to analyze whether the D/G intensity ratio changes as a function of both penetration depth and polarization for these data. Interestingly, this carbon nanotube was obtained from a different source than the previous nanotube examples (Figures 1A and 7A); hence there may be slight structural differences in this nanotube that lead to differences in the measured spectra.[59] These data indicate that optical spectroscopy/microscopy is an important complement to electron microscopy, revealing subtle differences in the spectral properties of the nanotube associated with structural features that cannot be resolved using standard high-resolution imaging techniques.

CONCLUSIONS

In this paper, we have presented a new approach for studying unenhanced Raman scattering from a single carbon nanotube with subdiffraction-limited resolution. By employing through-the-objective TIR Raman excitation coupled to an AFM, we are able to detect Raman scattering from a single suspended carbon nanotube without signal enhancement. Furthermore, we have shown that we can tune the penetration depth of the excitation field by steps as small as 2−10 nm, well below the diffraction limit of light, allowing us to probe length-dependent differences in the nanotube structure through changes in its Raman spectrum. By detecting the ratio of the D and G bands at different incident angles, we showed that defects are strongly localized on the end of the carbon nanotubes, demonstrating the ability of our approach to detect correlated chemical and structural changes at the nanoscale. Shifts in the Raman band frequencies were also observed at different penetration depths, although the origin of these shifts is still unclear. We have also shown that the polarization of the incident beam plays an important role in characterizing the nanotubes, both for exploring the orientation of defects along the nanotube axis as well as for characterizing local curvature or bending in the nanotubes. To summarize, we have presented a new strategy for studying the chemical and structural properties of suspended carbon nanotubes, and we believe that this method can be extended to study many other nanoscale/molecular systems in various environments, especially as AFM tip functionalization strategies become a more mature technology.

MATERIALS AND METHODS

Carbon Nanotube Functionalized AFM Tips. Multiwalled carbon nanotubes, 8−15 nm in diameter, were purchased from cheaptubes.com (sku-030102) and were used as received (for the nanotube tips presented in Figures 1B and 7A). Additional multiwalled carbon nanotubes were received from Xidex Corporation (the nanotube tip presented in Figure 7B). Gold-coated silicon AFM probes were purchased from Budget Sensors (Tap300GB) and were functionalized with single carbon nanotubes as described previously.[32] Briefly, the nanotubes were

mounted on the AFM probes by *in situ* manipulation in an SEM/FIB (FEI Strata DB235 SEM/FIB) equipped with a nanomanipulator (Zyvex s-prober). Each nanotube was welded to the AFM probe by e-beam deposition of platinum within the SEM and was checked for whether it fit the length requirements of our experiment (500−1000 nm) before use. Tips were imaged in the SEM both before and after use to ensure that no obvious damage or breakage occurred during AFM imaging.

Combined Optical Microscopy/Spectroscopy and AFM. A detailed description of the optical setup is provided in the Supporting Information. An AFM (NTEGRA Vita, NT-MDT) was mounted on top of an inverted optical microscope (Olympus IX-71), while the objective lens (Olympus 60×, NA = 1.45, TIRF oil immersion) was mounted at the base of the AFM to minimize noise (per the design of this AFM). Argon plasma was used to clean glass coverslips, which were used as substrates to provide an interface for TIR, as shown in Figure 1A. Silver colloids were drop cast from solution onto the cleaned glass coverslips to serve as focus markers for the experiment. An inorganic immersion liquid (Cargille OHZB) with refractive index of 1.5 was used instead of standard immersion oil (immersion oil is Raman-active and has a greater signal than a single suspended carbon nanotube) to provide contact between the objective and the glass coverslip. White light (Ocean Optics LS-1) TIR imaging was used to set the focus of the system by imaging the scattering from the silver colloids.[33] The nanotube tip was then mounted in the AFM and approached the surface. Since we can visually locate the position of the tip on the surface using white light TIR imaging,[33] it is possible to position the tip so it will be aligned to the center of the objective (by moving it with the AFM scanner). The nanotube was tapping at the same position during the measurements using the closed loop function of the AFM.

Raman scattering was excited by a 532 nm laser (CrystaLaser CL-2000) introduced *via* epi-illumination and a dichroic mirror into the NA 1.45 immersion objective. The scattered light was collected through the same objective, filtered through a notch filter (Semrock), and directed to the spectrometer (PI-Acton Spectra-Pro SP2500), equipped with a 1200 groove/mm grating. The dispersed light was then sent to a liquid nitrogen cooled camera (PI-Acton SPEC-10) for spectral acquisition. Raman spectra from single nanotubes were acquired for 30 s each with 10 summed accumulations. Background spectra were obtained under the same conditions by retracting the AFM tip from the surface; the background spectra were then subtracted to produce the final raw carbon nanotube Raman spectra (such as those shown in Figures 2, 6, and 7). No smoothing filter was applied or additional background subtraction was performed. Spectra were fit with eq 3 using homewritten MatLab code. The spectra were acquired at nonsequential penetration depths to prevent any artifacts due to continued use of the tip.

Acknowledgment. We thank R. Shaver for her assistance with early construction of our apparatus. We would also like to thank Xidex Corporation, Austin, Texas, for the contribution of carbon nanotubes. This work was supported with funding from DARPA (Grant No. N66001-09-1-2075) as well as start up funds from the University of Texas at Austin.

Supporting Information Available: Complete experimental setup, description of TIR angle of incidence calibration procedure, and model describing the effect of tip oscillation in an evanescent excitation field. This material is available free of charge *via* the Internet at http://pubs.acs.org.

REFERENCES AND NOTES

1. Friedrich, H.; de Jongh, P. E.; Verkleij, A. J.; de Jong, K. P. Electron Tomography for Heterogeneous Catalysts and Related Nanostructured Materials. *Chem. Rev.* **2009,** *109*, 1613–1629.
2. Flores, S. M.; Toca-Herrera, J. L. The New Future of Scanning Probe Microscopy: Combining Atomic Force Microscopy with Other Surface-Sensitive Techniques, Optical and Microscopy Fluorescence Techniques. *Nanoscale* **2009,** *1*, 40–49.
3. Novotny, L.; Stranick, S. J. Near-Field Optical Microscopy and Spectroscopy with Pointed Probes. *Annu. Rev. Phys. Chem.* **2006,** *57*, 303–331.
4. Dyba, M.; Hell, S. W. Focal Spots of Size Lambda/23 Open up Far-Field Fluorescence Microscopy at 33 nm Axial Resolution. *Phys. Rev. Lett.* **2002,** *88*, 163901.
5. Rust, M. J.; Bates, M.; Zhuang, X. W. Sub-Diffraction-Limit Imaging by Stochastic Optical Reconstruction Microscopy (STORM). *Nat. Methods* **2006,** *3*, 793–795.
6. Betzig, E.; Patterson, G. H.; Sougrat, R.; Lindwasser, O. W.; Olenych, S.; Bonifacino, J. S.; Davidson, M. W.; Lippincott-Schwartz, J.; Hess, H. F. Imaging Intracellular Fluorescent Proteins at Nanometer Resolution. *Science* **2006,** *313*, 1642–1645.
7. Zayats, A. V.; Sandoghdar, V. Apertureless Scanning Near-Field Second-Harmonic Microscopy. *Opt. Commun.* **2000,** *178*, 245–249.
8. Lewis, A.; Isaacson, M.; Harootunian, A.; Muray, A. Development of a 500-A Spatial-Resolution Light-Microscope 0.1. Light is Efficiently Transmitted through Gamma-16 Diameter Apertures. *Ultramicroscopy* **1984,** *13*, 227–231.
9. Betzig, E.; Lewis, A.; Harootunian, A.; Isaacson, M.; Kratschmer, E. Near Field Scanning Optical Microscopy (NSOM): Development and Biophysical Applications. *Biophys. J.* **1986,** *49*, 269–279.
10. Hartschuh, A. Tip-Enhanced Near-Field Optical Microscopy. *Angew. Chem., Int. Ed.* **2008,** *47*, 8178–8191.
11. Hell, S. W. Far-Field Optical Nanoscopy. *Science* **2007,** *316*, 1153–1158.
12. Stockle, R. M.; Suh, Y. D.; Deckert, V.; Zenobi, R. Nanoscale Chemical Analysis by Tip-Enhanced Raman Spectroscopy. *Chem. Phys. Lett.* **2000,** *318*, 131–136.
13. Hartschuh, A.; Beversluis, M. R.; Bouhelier, A.; Novotny, L. Tip-Enhanced Optical Spectroscopy. *Philos. Trans. R. Soc. London, Ser. A* **2004,** *362*, 807–819.
14. Kneipp, K.; Moskovits, M.; Kneipp, H.; Pettinger, B. T ip-Enhanced Raman Spectroscopy (TERS). In *Surface-Enhanced Raman Scattering*; Springer: Berlin/Heidelberg: 2006; Vol. 103, pp 217−240.
15. Sanchez, E. J.; Novotny, L.; Xie, X. S. Near-Field Fluorescence Microscopy Based on Two-Photon Excitation with Metal Tips. *Phys. Rev. Lett.* **1999,** *82*, 4014–4017.
16. Hoppener, C.; Novotny, L. Antenna-Based Optical Imaging of Single Ca^{2+} Transmembrane Proteins in Liquids. *Nano Lett.* **2008,** *8*, 642–646.
17. Mu, C.; Mangum, B. D.; Xie, C.; Gerton, J. M. Nanoscale Fluorescence Microscopy Using Carbon Nanotubes. *IEEE J. Sel. Top. Quantum Electron.* **2008,** *14*, 206–216.
18. Hoppener, C.; Novotny, L. Imaging of Membrane Proteins Using Antenna-Based Optical Microscopy. *Nanotechnology* **2008,** *19*, 384012.
19. Lahrech, A.; Bachelot, R.; Gleyzes, P.; Boccara, A. C. Infrared-Reflection-Mode Near-Field Microscopy Using an Apertureless Probe with a Resolution of Lambda/600. *Opt. Lett.* **1996,** *21*, 1315–1317.
20. Brehm, M.; Taubner, T.; Hillenbrand, R.; Keilmann, F. Infrared Spectroscopic Mapping of Single Nanoparticles and Viruses at Nanoscale Resolution. *Nano Lett.* **2006,** *6*, 1307–1310.
21. Akhremitchev, B. B.; Pollack, S.; Walker, G. C. Apertureless Scanning Near-Field Infrared Microscopy of a Rough Polymeric Surface. *Langmuir* **2001,** *17*, 2774–2781.
22. Hayazawa, N.; Inouye, Y.; Sekkat, Z.; Kawata, S. Near-Field Raman Imaging of Organic Molecules by an Apertureless Metallic Probe Scanning Optical Microscope. *J. Chem. Phys.* **2002,** *117*, 1296–1301.
23. Hartschuh, A.; Sanchez, E. J.; Xie, X. S.; Novotny, L. High-Resolution Near-Field Raman Microscopy of Single-Walled Carbon Nanotubes. *Phys. Rev. Lett.* **2003,** *90*, 095503.
24. Stranahan, S. M.; Willets, K. A. Super-Resolution Optical Imaging of Single-Molecule SERS Hot Spots. *Nano Lett.* **2010,** *10*, 3777–3784.

25. Javey, A.; Guo, J.; Farmer, D. B.; Wang, Q.; Wang, D. W.; Gordon, R. G.; Lundstrom, M.; Dai, H. J. Carbon Nanotube Field-Effect Transistors with Integrated Ohmic Contacts and High-k Gate Dielectrics. *Nano Lett.* **2004,** *4*, 447–450.
26. Zhang, D.; Ryu, K.; Liu, X.; Polikarpov, E.; Ly, J.; Tompson, M. E.; Zhou, C. Transparent, Conductive, and Flexible Carbon Nanotube Films and Their Application in Organic Light-Emitting Diodes. *Nano Lett.* **2006,** *6*, 1880–1886.
27. Endo, M.; Kim, Y. A.; Hayashi, T.; Nishimura, K.; Matusita, T.; Miyashita, K.; Dresselhaus, M. S. Vapor-Grown Carbon Fibers (VGCFs): Basic Properties and Their Battery Applications. *Carbon* **2001,** *39*, 1287–1297.
28. Ajayan, P. M.; Stephan, O.; Colliex, C.; Trauth, D. Aligned Carbon Nanotube Arrays Formed by Cutting a Polymer Resin—Nanotube Composite. *Science* **1994,** *265*, 1212–1214.
29. Peica, N.; Thomsen, C.; Maultzsch, J. Tip-Enhanced Raman Scattering along a Single Wall Carbon Nanotubes Bundle. *Phys. Status Solidi B* **2010,** *247*, 2818–2822.
30. Yano, T.-a.; Verma, P.; Saito, Y.; Ichimura, T.; Kawata, S. Pressure-Assisted Tip-Enhanced Raman Imaging at a Resolution of a Few Nanometres. *Nat. Photonics* **2009,** *3*, 473–477.
31. Cognet, L.; Tsyboulski, D. A.; Weisman, R. B. Subdiffraction Far-Field Imaging of Luminescent Single-Walled Carbon Nanotubes. *Nano Lett.* **2008,** *8*, 749–753.
32. Yu, M. F.; Lourie, O.; Dyer, M. J.; Moloni, K.; Kelly, T. F.; Ruoff, R. S. Strength and Breaking Mechanism of Multiwalled Carbon Nanotubes under Tensile Load. *Science* **2000,** *287*, 637–640.
33. Stiles, R. L.; Willets, K. A.; Sherry, L. J.; Roden, J. M.; Van Duyne, R. P. Investigating Tip-Nanoparticle Interactions in Spatially Correlated Total Internal Reflection Plasmon Spectroscopy and Atomic Force Microscopy. *J. Phys. Chem. C* **2008,** *112*, 11696–11701.
34. Axelrod, D.; Burghardt, T. P.; Thompson, N. L. Total Internal-Reflection Fluorescence. *Annu. Rev. Biophys. Bioeng.* **1984,** *13*, 247–268.
35. Mckee, K. J.; Smith, E. A. Development of a Scanning Angle Total Internal Reflection Raman Spectrometer. *Rev. Sci. Instrum.* **2010,** *81*, 043106.
36. Alexa, L. M.; Daniel, A. Direct Measurement of the Evanescent Field Profile Produced by Objective-Based Total Internal Reflection Fluorescence. *J. Biomed. Opt.* **2006,** *11*, 014006.
37. Rothschild, A.; Cohen, S. R.; Tenne, R. WS_2 Nanotubes as Tips in Scanning Probe Microscopy. *Appl. Phys. Lett.* **1999,** *75*, 4025–4027.
38. Kaplan-Ashiri, I.; Cohen, S. R.; Gartsman, K.; Rosentsveig, R.; Seifert, G.; Tenne, R. Mechanical Behavior of Individual WS_2 Nanotubes. *J. Mater. Res.* **2004,** *19*, 454–459.
39. Dresselhaus, M. S.; Jorio, A.; Hofmann, M.; Dresselhaus, G.; Saito, R. Perspectives on Carbon Nanotubes and Graphene Raman Spectroscopy. *Nano Lett.* **2010,** *10*, 751–758.
40. Dresselhaus, M. S.; Dresselhaus, G.; Saito, R.; Jorio, A. Raman Spectroscopy of Carbon Nanotubes. *Phys. Rep.* **2005,** *409*, 47–99.
41. Dresselhaus, M. S. NT10: Recent Advances in Carbon Nanotube Science and Applications. *ACS Nano* **2010,** *4*, 4344–4349.
42. Jorio, A.; Pimenta, M. A.; Souza, A. G.; Saito, R.; Dresselhaus, G.; Dresselhaus, M. S. Characterizing Carbon Nanotube Samples with Resonance Raman Scattering. *New J. Phys.* **2003,** *5*, 139.
43. Maejima, K.; Suzuki, O.; Uchida, T.; Aoki, N.; Tachibana, M.; Ishibashi, K.; Ochiai, Y. Raman and Transport Studies in Multi-Walled Carbon Nanotubes. *J. Phys. Conf. Ser.* **2006,** *38*, 33.
44. Minati, L.; Speranza, G.; Bernagozzi, I.; Torrengo, S.; Toniutti, L.; Rossi, B.; Ferrari, M.; Chiasera, A. Investigation on the Electronic and Optical Properties of Short Oxidized Multiwalled Carbon Nanotubes. *J. Phys. Chem. C* **2010,** *114*, 11068–11073.
45. Joh, D. Y.; Herman, L. H.; Ju, S.-Y.; Kinder, J.; Segal, M. A.; Johnson, J. N.; Chan, G. K. L.; Park, J. On-Chip Rayleigh Imaging and Spectroscopy of Carbon Nanotubes. *Nano Lett.* **2010**10.1021/nl1012568.
46. Choi, J. H.; Strano, M. S. Solvatochromism in Single-Walled Carbon Nanotubes. *Appl. Phys. Lett.* **2007,** *90*, 223114.
47. Kim, D. Y.; Yun, Y. S.; Bak, H.; Cho, S. Y.; Jin, H. J. Aspect Ratio Control of Acid Modified Multiwalled Carbon Nanotubes. *Curr. Appl. Phys.* **2010,** *10*, 1046–1052.
48. Spudat, C.; Meyer, C.; Schneider, C. M. Oxidation Induced Shifts of Raman Modes of Carbon Nanotubes. *Phys. Status Solidi B* **2008,** *245*, 2205–2208.
49. Chakrabarti, S.; Gong, K.; Dai, L. Structural Evaluation along the Nanotube Length for Super-Long Vertically Aligned Double-Walled Carbon Nanotube Arrays. *J. Phys. Chem. C* **2008,** *112*, 8136–8139.
50. Minati, L.; Speranza, G.; Bernagozzi, I.; Torrengo, S.; Toniutti, L.; Rossi, B.; Ferrari, M.; Chiasera, A. Investigation on the Electronic and Optical Properties of Short Oxidized Multiwalled Carbon Nanotubes. *J. Phys. Chem. C* **2010,** *114*, 11068–11073.
51. Costa, S.; Scheibe, B.; Rummeli, M.; Borowiak-Palen, E. Raman Spectroscopy Study on Concentrated Acid Treated Carbon Nanotubes. *Phys. Status Solidi B* **2009,** *246*, 2717–2720.
52. Park, J. S.; Sasaki, K.; Saito, R.; Izumida, W.; Kalbac, M.; Farhat, H.; Dresselhaus, G.; Dresselhaus, M. S. Fermi Energy Dependence of the G-Band Resonance Raman Spectra of Single-Wall Carbon Nanotubes. *Phys. Rev. B* **2009,** *80*, 081402.
53. Puech, P.; Flahaut, E.; Bassil, A.; Juffmann, T.; Beuneu, F.; Bacsa, W. S. Raman Bands of Double-Wall Carbon Nanotubes: Comparison with Single- and Triple-Wall Carbon Nanotubes, and Influence of Annealing and Electron Irradiation. *J. Raman Spectrosc.* **2007,** *38*, 714–720.
54. Thomsen, C.; Reich, S.; Maultzsch, J. Resonant Raman Spectroscopy of Nanotubes. *Philos. Trans. R. Soc. London* **2004,** *362*, 2337–2359.
55. Puech, P.; Anwar, A. W.; Flahaut, E.; Dunstan, D. J.; Bassil, A.; Bacsa, W. Raman G and D Band in Strongly Photoexcited Carbon Nanotubes. *Phys. Rev. B* **2009,** *79*, 085418.
56. Nii, H.; Sumiyama, Y.; Nakagawa, H.; Kunishige, A. Influence of Diameter on the Raman Spectra of Multi-Walled Carbon Nanotubes. *Appl. Phys. Express* **2008,** *1*, 064005.
57. Thomsen, C.; Reich, S.; Jantoljak, H.; Loa, I.; Syassen, K.; Burghard, M.; Duesberg, G. S.; Roth, S. Raman Spectroscopy on Single- and Multi-Walled Nanotubes under High Pressure. *Appl. Phys. A* **1999,** *69*, 309–312.
58. Duesberg, G. S.; Loa, I.; Burghard, M.; Syassen, K.; Roth, S. Polarized Raman Spectroscopy on Isolated Single-Wall Carbon Nanotubes. *Phys. Rev. Lett.* **2000,** *85*, 5436–5439.
59. Grobert, N. Carbon Nanotubes—Becoming Clean. *Mater. Today* **2007,** *10*, 28–35.